

## RESEARCH ARTICLE

# Sub-seasonal prediction of rainfall over the South China Sea and its surrounding areas during spring–summer transitional season

Qingquan Li<sup>1,2</sup>  | Juanhuai Wang<sup>3</sup> | Song Yang<sup>4,5,6</sup>  | Fang Wang<sup>1,2</sup> | Jie Wu<sup>1</sup> | Yamin Hu<sup>3</sup>

<sup>1</sup>Laboratory for Climate Studies, National Climate Center, China Meteorological Administration, Beijing, China

<sup>2</sup>Key Laboratory of Meteorological Disaster, Ministry of Education/Joint International Research Laboratory of Climate and Environment Change/Collaborative Innovation Center on Forecast and Evaluation of Meteorological Disasters, Nanjing University of Information Science & Technology, Nanjing, China

<sup>3</sup>Guangdong Climate Center, Guangdong Province, Guangzhou, China

<sup>4</sup>School of Atmospheric Sciences, Sun Yat-sen University, Guangzhou, China

<sup>5</sup>Guangdong Province Key Laboratory for Climate Change and Natural Disaster Studies, Sun Yat-sen University, Guangzhou, China

<sup>6</sup>Southern Marine Science and Engineering Guangdong Laboratory (Zhuhai), Guangdong, China

## Correspondence

Juanhuai Wang, Guangdong Climate Center, Guangdong Province, Guangzhou, China.

Email: wangjh0104@foxmail.com

Song Yang, School of Atmospheric Sciences, Sun Yat-sen University, Guangzhou, China.

Email: yangsong3@mail.sysu.edu.cn

## Funding information

Strategic Priority Research Program of Chinese Academy of Sciences, Grant/Award Number: XDA20100304; National Key Scientific Research Plan of China, Grant/Award Numbers: 2016YFA0602200, 2013CB430202; National Natural Science Foundation of China, Grant/Award Number: 41661144019; Jiangsu Collaborative Innovation Center for Climate Change

## Abstract

The sub-seasonal characteristics and prediction of rainfall over the South China Sea and surrounding areas during spring–summer transitional season (April–May–June) are investigated using a full set of hindcasts generated by the Dynamic Extended Range Forecast operational system version 2.0 (DERF2.0) of Beijing Climate Center, China Meteorological Administration. The onset and development of Asian summer monsoon and the seasonal migration of rain belt over East Asia can be well depicted by the model hindcasts at various leads. However, there exist considerable differences between model results and observations, and model biases depend not only on the lead time, but also on the stage of monsoon evolution. In general, forecast skill drops with increasing lead time but rises again after lead time becomes longer than 30 days, possibly associated with the effect of slowly-varying forcing or atmospheric variability. An abrupt turning point of bias development appears around mid-May when bias growths of wind and precipitation exhibit significant changes over the northwestern Pacific and South Asia, especially over the Bay of Bengal and the South China Sea. This abrupt bias change is reasonably captured by the first two modes of multivariate empirical orthogonal function analysis, which reveals several important features associated with the bias change. This analysis may provide useful information for further improving model performance in sub-seasonal rainfall prediction.

This is an open access article under the terms of the Creative Commons Attribution-NonCommercial-NoDerivs License, which permits use and distribution in any medium, provided the original work is properly cited, the use is non-commercial and no modifications or adaptations are made.

© 2019 The Authors. International Journal of Climatology published by John Wiley & Sons Ltd on behalf of the Royal Meteorological Society.

**KEYWORDS**

east-southeast Asian monsoon rainfall, spring–summer transitional season, sub-seasonal prediction

**1 | INTRODUCTION**

Numerical models have been applied in operational climate prediction and climate change research since decades ago (Sperber and Palmer, 1996; Johns *et al.*, 2006). However, these models often show deficiencies in reproducing realistic climatology, and their prediction capability is inevitably limited (Li and Zhao, 2002; Li *et al.*, 2004; Zhou *et al.*, 2009a; 2009b; 2009c; Lee *et al.*, 2010; Li *et al.*, 2010; Zhou and Zou, 2010). At present, climate system models are still not perfect, and their forecast skills cannot meet the governmental and social demands. Thus, assessing the skills of dynamical prediction, understanding models' systematic biases, and providing useful information for improving these models and their prediction capability is of critical importance for both academic and operational communities (Zhu *et al.*, 2013; Li *et al.*, 2015; Wei *et al.*, 2017).

One of the recent research hotspots is the 10–30-day forecast with a focus on the extended-range time scale between weather phenomena and seasonal mean, which is of great significance to disaster prevention and mitigation. However, our current skills cannot fulfil the need for operational climate prediction due to initial errors and the deficiencies of models themselves: many models show limited skills in simulating and predicting sub-seasonal variability. Thus, assessing and improving the skills of 10–30-day forecast have become a challenging and important task in both operational forecast sector and academic community. Previous studies have shown that the skill of dynamical extended-period prediction is not significantly better than that of statistical persistent prediction, although the former coincidentally achieves a high forecasting skill score sometimes (Molteni *et al.*, 1986; Anderson and Van, 1994). On the other hand, studies have also found that some state-of-the-art global models exhibit useful skills on time scales beyond 2–3 weeks, especially when measured by indices of multivariate spatial modes (Fu *et al.*, 2013; Neena *et al.*, 2014). Recently, Abhilash *et al.* (2014) and Liu *et al.* (2014a) examined the sub-seasonal prediction skill of the NCEP CFSv2 for the Indian monsoon and the major global monsoon components and found that the actual forecast skill was closely related to the behaviours of large-scale features of the monsoons. Meanwhile, the sub-seasonal predictions of regional summer rainfall over several tropical Asian ocean and land domains were examined using the CFSv2 (Liu *et al.*, 2013; 2015) and it was noted that

the forecast skills exhibited geographical differences, with higher skills for oceans than for land.

The Dynamic Extended Range Forecast operational system version 2.0 (DERF2.0) of the Beijing Climate Center (BCC) of China is one of the state-of-the-art operational seasonal prediction systems. In recent years, the DERF2.0 forecasts have achieved great progress with the upgrade from DERF1.0 to DERF2.0, and become an important tool in research and prediction operation. The major upgrade in DERF from version 1 to version 2 is the climate model. DERF 1.0 utilizes the Beijing Climate Center (BCC) Atmospheric General Circulation Model (AGCM) version 1.0 (BCC\_AGCM 1.0), which is triangularly truncated with 63 waves ( $\sim 1.875^\circ$ ) in the horizontal direction and 16 layers in the vertical direction (Ding *et al.*, 2002). DERF2.0 is established on the basis of BCC\_AGCM2.2 (T106 L26), which has a horizontal T106 truncation ( $\sim 1.125^\circ$ ) and 26 layers in the vertical (Wu *et al.*, 2010). He *et al.* (2014) found that the DERF2.0 performances for temperature and precipitation predictions were significantly better than the DERF1.0. The DERF2.0 was even somewhat skillful in predicting extreme droughts and floods, such as those in 1998 and 2006. However, the DERF2.0 still has apparent deficiencies in reproducing the observed climatology, variability, and relationships with other climate systems. Especially, DERF2.0 predictions are often less skillful in capturing regional characteristics compared to large-scale features (Chen *et al.*, 2016; Zhang and Chen, 2016; Li *et al.*, 2017), and it is also more difficult to predict rainfall variability compared to circulation variability (Tang *et al.*, 2016) by the DERF2.0 model. In addition, the skill for monthly-mean precipitation forecast is better than that for daily-mean precipitation, and it is the same for low-intensity rainfall than for high-medium-intensity rainfall (Liu *et al.*, 2014a).

The months from April to June are the main period for the onset, development, and prevalence of the East Asian summer monsoon, and for the 'pre-flood season' in South China, where the precipitation from April to June accounts for 40–50% of the annual amount (Huang, 1986). Thus, an accurate forecast in this period plays an important role in the overall climate prediction. Moreover, during this period of spring-to-summer transition when the atmospheric circulation bears abrupt changes (Wu *et al.*, 2010), heavy flood events resulted from large precipitation variability occur frequently in Southeast China. The prediction skill during the spring–summer

transition, however, is quite low. To make things worse, less attention is paid to the climate prediction for the spring-to-summer transition. Therefore, it is significant to discuss the characteristics of precipitation from April to June and to evaluate the skill of precipitation prediction by dynamical forecast system.

The differences between DERF2.0 and observations on the sub-seasonal scale are less discussed compared to those on monthly and/or seasonal scales during the period of spring-to-summer transition. There is limited exploration over the South China Sea (SCS) and its surrounding areas, which is an important aspect to address in this study. Therefore, here we diagnose the prediction biases of precipitation, 850-hPa winds, and skin temperature (SKT) during the spring-to-summer transition by the DERF2.0 on sub-seasonal scale, and investigate the key factors that affect prediction skills. Several analyses are conducted to address the following questions. What, when, and where are the conspicuous biases in the sub-seasonal predictions of precipitation, 850-hPa winds, and SKT over the SCS and its surrounding areas? How different are the biases during different stages of seasonal evolution and as a function of lead time? At which lead time can the sub-seasonal regional rainfall variability be predicted? What are the possible physical causes of these differences?

The focuses of this study are mainly the pentad climatic anomalies (such as 5-day average rainfall anomalies). In order to reveal and understand the sources of prediction errors, the predictions of related circulations are analysed. Extended-range forecast requires that a model can predict the monthly climate background well, and capture the climate prediction on a relatively short time scale for a stable forecast. Therefore, we first analyse the monthly average climate state of the model in order to verify the basic performance of the model.

The article is organized as follows. In Section 2, we describe the model, observation data, and the analysis methods applied in this study. In Section 3, we discuss the predictions of monthly climatological features, sub-seasonal evolution of winds and rainfall over the SCS and its surrounding areas, the forecast skills over selected regions, and possible causes of biases. Summary and concluding remarks are provided in Section 4.

## 2 | DATA AND METHODOLOGY

### 2.1 | Model and hindcast outputs

In this study, the hindcast outputs from the DERF2.0 are analysed. The availability of comprehensive retrospective forecasts from the DERF2.0 offers an opportunity to

understand the predictability of precipitation, winds, SKT, etc. In the DERF2.0 system, the global atmospheric circulation model BCC\_AGCM2.2 (T106 L26) is utilized to generate the extended range (sub-seasonal) climate prediction based on a two-tier method. The BCC\_AGCM2.2 model is integrated under the forcing of a given sea surface temperature (SST), composing the observed SST anomaly of the initial time and the climatological mean SST. The initial conditions for atmosphere and SST are obtained from the NCEP/NCAR reanalysis (Kalnay *et al.*, 1996) and the Optimum Interpolation Sea Surface Temperature (OISST) of the National Oceanic and Atmospheric Administration (NOAA; Reynolds *et al.*, 2002), respectively. Four model runs (00Z, 06Z, 12Z, and 18Z) are initialized every day starting on January 1, 1983, and run for 56- or 57-day integrations each. Daily mean is generated as the ensemble average of the four members. Daily- and monthly-averaged rainfall, 850- and 200-hPa winds, and SKT are analysed in this study.

### 2.2 | Observational data

Daily winds and SKT of the ERA-Interim reanalysis data are from the European Centre for Medium-range Weather Forecasts (ECMWF; Simmons *et al.*, 2007; Uppala *et al.*, 2008), with a horizontal resolution of  $0.75^\circ \times 0.75^\circ$ . The monthly precipitation of the Global Precipitation Climatology Project (GPCP; Huffman *et al.*, 2001) from 1983 to 2014 and the daily precipitation of the GPCP from 1997 to 2014 are used. These reanalysis data are referred to as observational data. For the convenience of comparison, all data are interpolated onto the resolution of  $1^\circ \times 1^\circ$  using the bilinear interpolation method.

### 2.3 | Analysis methods

The prediction skills during April–June, the spring-to-summer transition period, at various lead days (LD) for sub-seasonal prediction are examined. Monthly and pentad means are also analysed to exhibit both overall background and detailed evolution of biases. For a specific target month (or pentad) to predict, lead 0 is defined as the model run initialized on the first day of the month (or pentad), lead 1 denotes the model run initialized on the last day of the previous month (or pentad), lead 2 is for the forecast initialized on the last but 1 day of the previous month (or pentad), and so forth, until 26- or 27-lead days and 51- or 52-lead days for monthly mean and pentad mean prediction, respectively. In this article, we only analyse the hindcast data of 0–14 lead days for monthly mean and 0–49 lead days for pentad mean predictions as examples. The prediction for a certain month

is an ensemble mean of 60 members lead from 0 to 14 days (four members per day). The ensemble forecasts for a certain pentad are divided into 10 groups according to lead time, that is, 0–4, 5–9, 10–14, and every 5 days to 45–49 days. For example, for the target pentad of the first pentad of April, ensemble-mean prediction on the first day of April and the last 4 days of March is defined as the 0–4 day-lead (LD0-4) prediction. The pentad predictions are ensemble means of 20 members within 5-day-lead time. The statistical analysis methods used in this study include pattern correlation coefficient (PCC), anomaly correlation coefficient (ACC), Taylor diagram, and multivariate empirical orthogonal function (MV\_EOF) analysis. The Student's  $t$  test and the  $F$  test are used for statistical significance test.

### 3 | RESULT ANALYSIS

#### 3.1 | Monthly prediction skill

To understand the overall background of prediction biases, we present in Figure 1 the climatology of monthly precipitation and 850-hPa winds from observations and DERF2.0 prediction from April to June, as well as their differences. The ensemble means of 0–14 lead-day prediction for various target months are discussed. Overall, the main locations of forecasted rainfall agree well with those observed. The model captures the major evolution features of the Asian monsoon; that is, the rain belt associated with the intertropical convergence zone (ITCZ) strengthens gradually over the SCS and the western

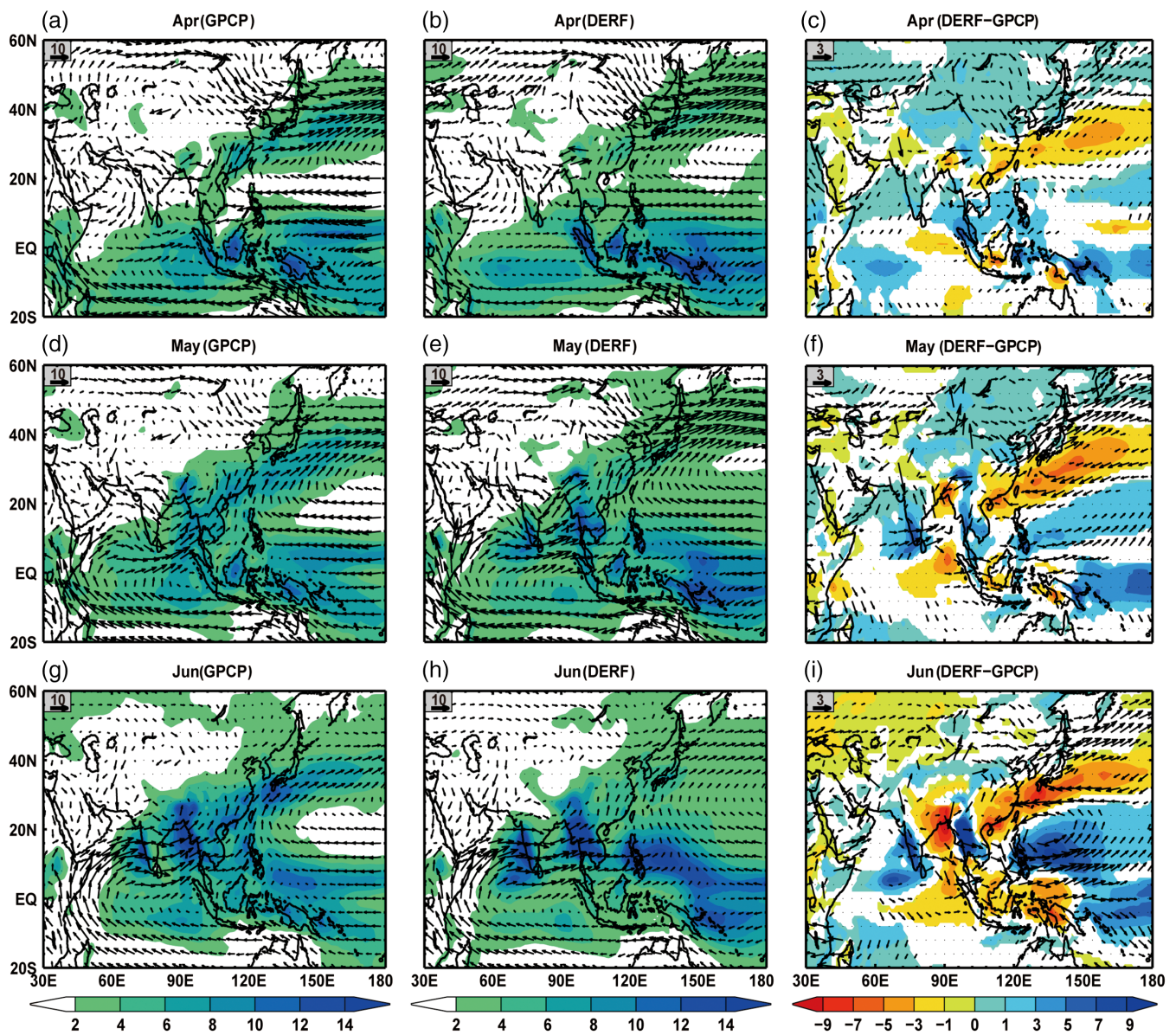


**FIGURE 1** Monthly precipitation (shading; units:  $\text{mm}\cdot\text{day}^{-1}$ ) and 850-hPa wind (vector; units:  $\text{m}\cdot\text{s}^{-1}$ ) for observations (left column), DERF2.0 predictions (middle column), and their differences (right column; predictions minus observations) from April to June (top to bottom). Only the differences passing the significant test of 95% confidence level (Student's  $t$  test for precipitation and  $F$  test for wind) are shown

tropical Pacific from April to June. In May, the Asian summer monsoon (ASM) occurs first around the Indo-China Peninsula (ICP) and Eastern Bay of Bengal, accompanied by apparently increased rainfall. In June, as the Indian summer monsoon starts, tropical westerly wind and precipitation develop and prevail, and the rain belt expands northward. Moreover, the westerly jet over the Arabian Sea enhances in May and June.

Apparently systematic biases, however, appear in the middle and lower latitudes, including the northerly wind bias over the equatorial Indian Ocean (IO), the westerly wind bias over the Indian Peninsula (IP) and ICP, and the cyclonic and anticyclonic wind biases over the northwestern Pacific Ocean (NWP), with most significant biases in June. Associated with the anticyclonic bias over Southeast China-Japan, there is an underestimation of rainfall from April to June. Dry biases appear over most parts of South China, the southern edge of the Tibetan Plateau (TP), the northern part of the Bay of Bengal (BOB), and the eastern equatorial IO. On the other hand, wet biases appear over ICP and IP, due possibly to the unreasonable estimate of the influence by topography in the model. These biases gradually increase from April to June. In addition, the biases can change their sign with time. For example, the wet bias in the ITCZ over SCS and tropical western Pacific in April is replaced by a dry bias in June.

The above analysis indicates that the hindcast results of precipitation are related to the circulation biases of the model. Then, what causes circulation biases? Since the thermodynamic difference between land and oceans is an essential factor that results in the monsoon and its variability, it is important to investigate the ability of the model to simulate the features of temperature, especially at the low levels. Indeed, Chen *et al.* (1997) found that the simulation bias of temperature might be one of the reasons that cause the biases of monsoon circulation. A

poor simulation of SST may also result in bad simulations of monsoon precipitation (Zhou and Yu, 2006). Therefore, to better understand the biases of monsoon precipitation, SKT (SST for oceans) is selected for a comparative analysis. The simulated SKT is more consistent with observation, compared to precipitation and winds. The model can reasonably depict the increase in skin temperature from April to June, as well as from the lower to higher latitudes, as in the observation (figure not shown). Figure 2 showing the differences in surface temperature between hindcast and observation, indicates warm biases in South Asia and most parts of East China including IP, ICP, and South China. Especially, almost all East China experiences significant warm biases in June, while most land areas from Northwest China to Northeast China are mainly dominated by cold biases. In addition, the cold biases around Lake Balkhash in April are replaced by warm biases from May to June, and the cold bias is more significant over land than over oceans, especially over the TP where the cold bias is apparently large. Although during summer months the TP is much warmer than the oceans, thus cold bias in TP can lead to weaker temperature differences between oceans and land and affect the intensity of monsoon circulation.

### 3.2 | Variation of sub-seasonal evolution

The development of ASM on the pentad time scale is investigated. We use pentad mean precipitation above  $6 \text{ mm}\cdot\text{day}^{-1}$  and 850 hPa zonal wind turning from easterly wind to westerly wind to define the ASM onset (Lau and Yang, 1997; Liu and Ding, 2007). Figure 3 shows the changes in observed precipitation before and after the onset of the ASM, which are the same as those in Figure 1a,d,g but on the pentad time scale. The monsoon onset over the Eastern Indian Ocean and Sumatra starts

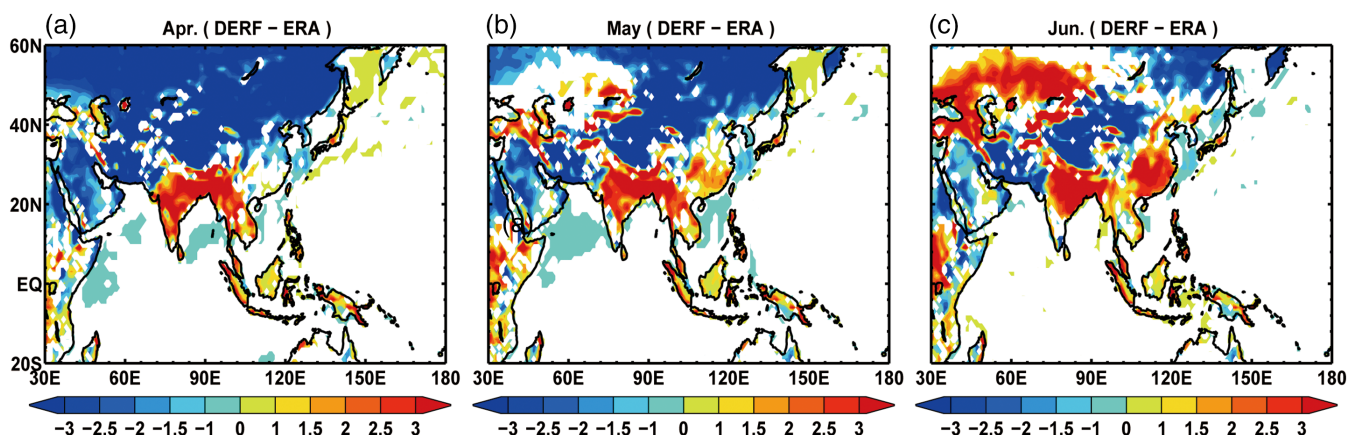


**FIGURE 2** Differences in monthly skin temperature (units:  $^{\circ}\text{C}$ ) between DERF2.0 predictions and observations (prediction minus observation) from April to June (left to right). Only the differences passing the significant test of 95% confidence level (Student's *t* test) are shown

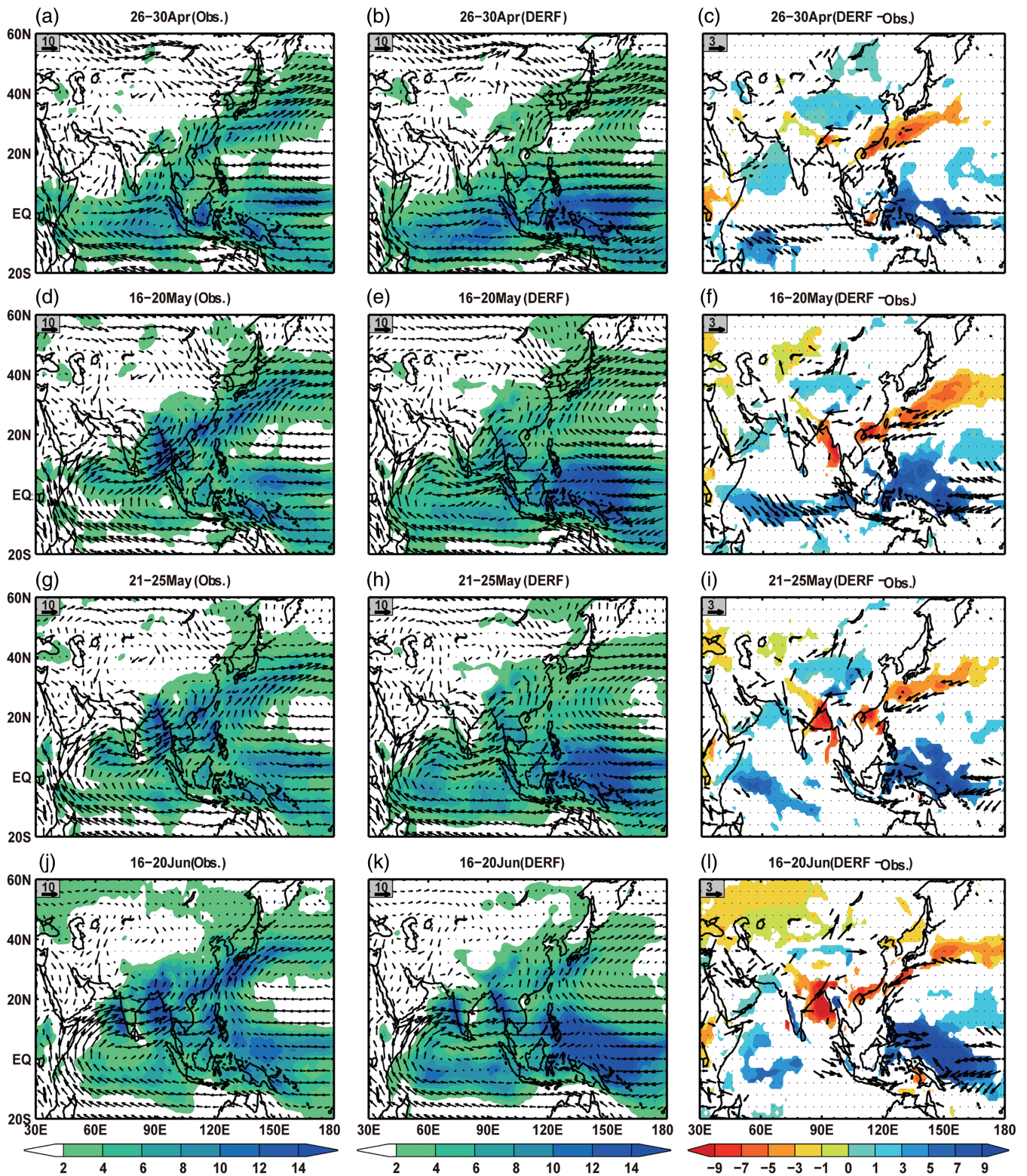


**FIGURE 3** Same as Figure 1, except for pentad precipitation (shading; units:  $\text{mm}\cdot\text{day}^{-1}$ ) and 850-hPa wind (vectors; units:  $\text{m}\cdot\text{s}^{-1}$ ) of the ensemble means of 0–4-day-lead predictions and observations from late spring to early summer (top to bottom). Only the differences passing the significant test of 95% confidence level (Student's  $t$  test for precipitation and  $F$  test for wind) are shown

from late April, following a northeastward movement of rain belt and being accompanied by prevailing southwesterly wind. However, the cross-equatorial flow is weak due to the control of northwesterly or northeasterly wind over the IP and the Arabian Sea (Figure 3a). The Eastern BOB and ICP summer monsoon establish in early May, accompanied by a gradual strengthening of southwesterly flow of the Somalia jet and a northward movement of equatorial convergence zone (figure not shown). Around mid-May, water vapour is transported from the southern IO to the Arabian Sea through the Somali jet and then to the SCS through BOB and ICP. The wind over the SCS turns from southeasterly to southwesterly in the fourth pentad of May (Figure 3d). Afterward, the onset of the SCS summer monsoon (SCSSM) in the fifth pentad of May (Figure 3g) marks the arrival of summer monsoon and the beginning of rainy season over East and Southeast Asian (Chen *et al.*, 2000; Ding *et al.*, 2006). Thus, gradual increases in precipitation occur over the BOB, ICP, SCS, and South China, as well as the Kuroshio area, in the fifth pentad of May, which agrees with the results of Zhao *et al.* (2007), He *et al.* (2008), and Qi *et al.* (2008). Accompanied by the onset of Indian summer monsoon, rain belt moves to the Yangtze River basin in mid-June, indicating the beginning of the Meiyu season (Figure 3j). Two separate rain belts then appear over East Asia: one is the ITCZ rain belt over the SCS-western tropical Pacific and the other is the convergence zone of Meiyu rain belt in East Asia. The evolution of these two rain belts is independent of each other.

Next, the variations of pentad rainfall and winds in DERF2.0 predictions are examined. Figure 3 shows the differences in pentad mean precipitation and 850-hPa winds between the ensemble means of 0–4-day-lead predictions and observations from April to June. The pentad predictions can generally capture the major evolution features of the ASM in observations. However, there are some significant systematic biases, especially in the magnitude of major rainfall centres. Similar to the features shown in Figure 1, there exist northerly wind bias over the equatorial region and cyclonic wind bias over the NWP in different stages during the spring-to-summer transition. Correspondingly, dry biases dominate in the southern flank of the TP, South China, and the Kuroshio region, while wet biases occur over the western Pacific and the southern IO. Interestingly, the biases of model predictions are closely related to the onset and the position of the ASM: the dry biases over BOB and SCS begin to propagate and become significant in the fourth and fifth pentads of May, respectively, along with the increasing easterly or northeasterly wind biases over the two regions (Figure 3f,i). The wet bias becomes significant in the fourth pentad of June over the western IP (Figure 3l),

which is perhaps due to the underestimate of the winds after monsoon onset. In addition, the magnitude and range of biases are consistent with the location and changing time of the rain belt (Figure 3f). For example, the region where rainfall is underestimated further shifts northward, along with the northward movement of Meiyu convergence zone rain belt in East Asia, while the range and magnitude of wet biases increase due to the northward shift of the northwestern Pacific subtropical high and the increase in cyclonic bias.

Figure 4, which shows the predictions at 25–29 lead days, indicates that the model can reproduce the development process of the ASM, but the precipitations over several key regions including IP, ICP, BOB, SCS, and South China and the Meiyu rain belt in East Asia exhibit larger biases at 25–29 lead days than at 0–4 lead days. Conversely, there are weaker wind biases in long-lead predictions than in shorter-lead predictions over many regions. From the shortest-lead (0–4 days) to the mid-lead (25–29 days) predictions, the northerly wind biases over the equatorial IO are significantly weaker. The cyclonic wind biases over the western Pacific are weaker in April and May, resulting in a remarkable decline of wet bias. The centre of the cyclonic bias shifts northward in June, bringing about the northward shift of the centre of wet bias. Nevertheless, there are opposite biases at the lead time of 25–29 days compared with the lead time of 0–4 days over some regions. For example, a weak dry bias appears over the southeastern Arabian Sea with short leads and it becomes a wet bias at longer leads, related possibly to the obvious cyclonic bias at the lead time of 25–29 days over the Arabian Sea. Meanwhile, the equatorial areas including the equatorial IO and the Maritime Continent show dry biases at the lead time of 25–29 days in June, while showing wet biases at the lead time of 0–4 days. Figure 4 also shows that the predictions at 45–49 lead days may not be skillful, but is helpful for revealing the growth of biases with increasing lead time. Correspondingly, the predictions at the 45–49 lead days are consistent with those at the 25–29 lead days, in terms of not only the time when the difference occurs, but also the position where the difference appears, except for the increasing degree of deviation.

The cross section of differences between observed and predicted pentad mean precipitations and 850-hPa zonal winds, at different lead days along 70°–90°E, 90°–110°E, and 110°–130°E are analysed respectively (Figures 5–7). The forecasted precipitation along 70°–90°E is characterized by a northward shift from the equator to the Asian continent and from the first pentad of April to the last pentad of June, which is consistent with the observed features (not shown). However, the model biases increase with lead time as shown in Figure 5. At first, the 0–4

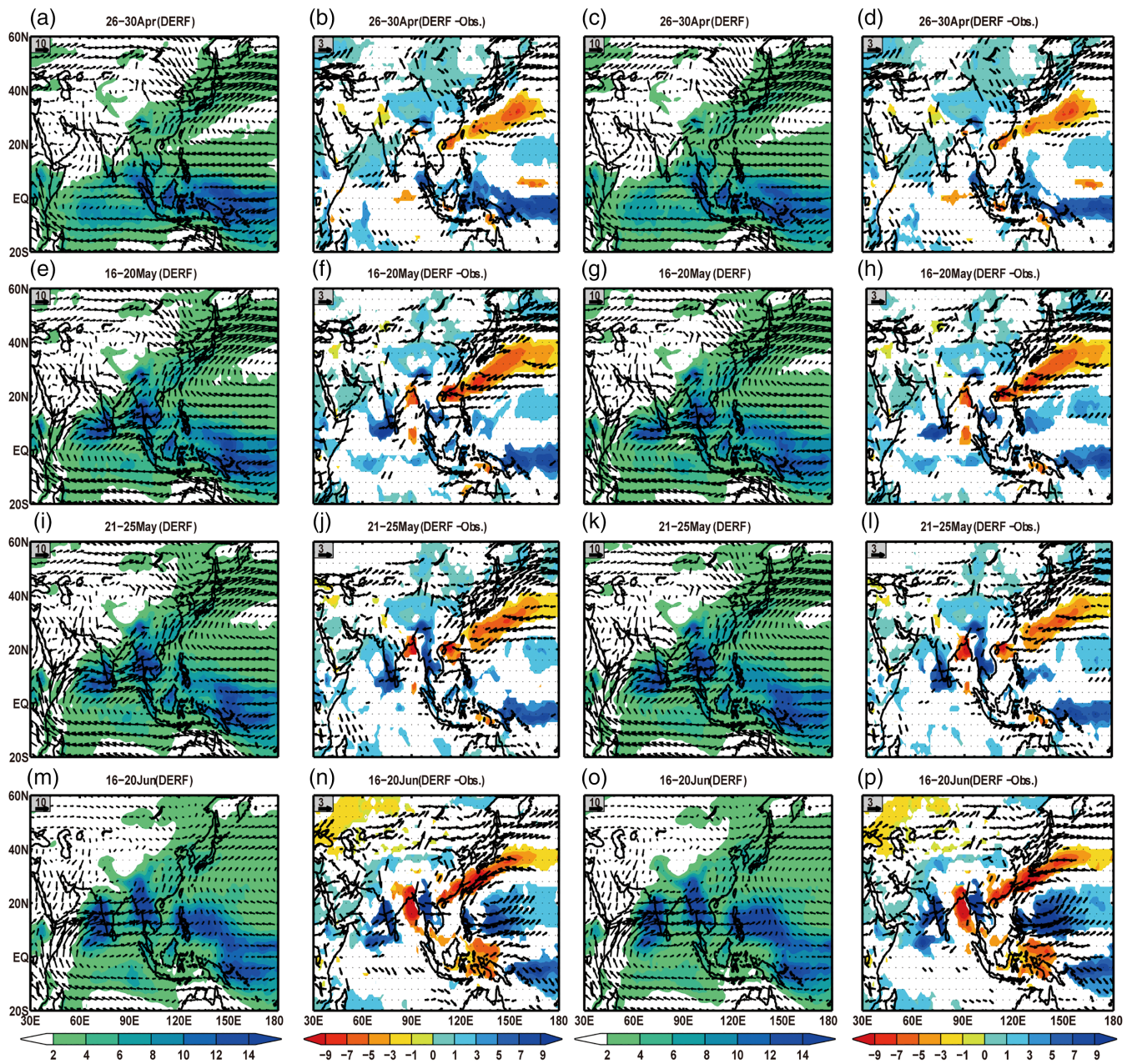


**FIGURE 4** Same as middle and right columns of Figure 3, except for the ensemble predictions with lead times from 25 to 29 days (two left columns) and from 45 to 49 days (two right columns). Only the differences passing the significant test of 95% confidence level (Student's  $t$  test for precipitation and  $F$  test for wind) are shown in the second and fourth columns

lead-day forecasts display small deviations from observations before June. The deviations increase slightly with increasing lead time as shown in Figure 3l, that is, the prediction skill decreases after the onset of the Indian monsoon. Then, the biases show a more consistent 'dry-wet-dry' feature from the equator to the Asian continent, and the dry biases gradually diminish while wet biases increase from 5–9 to 45–49 lead days especially in June. Consistent with the characteristics of precipitation change, the 0–4-day-lead forecasts of 850-hPa zonal wind

also display agreements with observations before June (Figure 5a). However, westerly biases gradually increase from 5–9 to 45–49 lead days around  $10^{\circ}\text{N}$  from April to June, which corresponds to an overestimate of rainfall (Figure 5b–d). This feature indicates that the overestimate of precipitation may be due to the bias in 850-hPa westerly wind.

The model can well capture the observed feature of precipitous increase in precipitation along  $90^{\circ}$ – $110^{\circ}\text{E}$  after the onset of BOB monsoon around the third pentad

**FIGURE 5** Latitude-time cross sections of differences in precipitation (shading; units:  $\text{mm}\cdot\text{day}^{-1}$ ) and 850-hPa zonal wind (contour; units:  $\text{m}\cdot\text{s}^{-1}$ ) between ensemble predictions and observations along  $70^\circ\text{--}90^\circ\text{E}$ . the solid and dotted lines denote the positive and negative values, respectively. (a), (b), (c), and (d) for 0–4, 5–9, 15–19, 45–49 lead day prediction, respectively

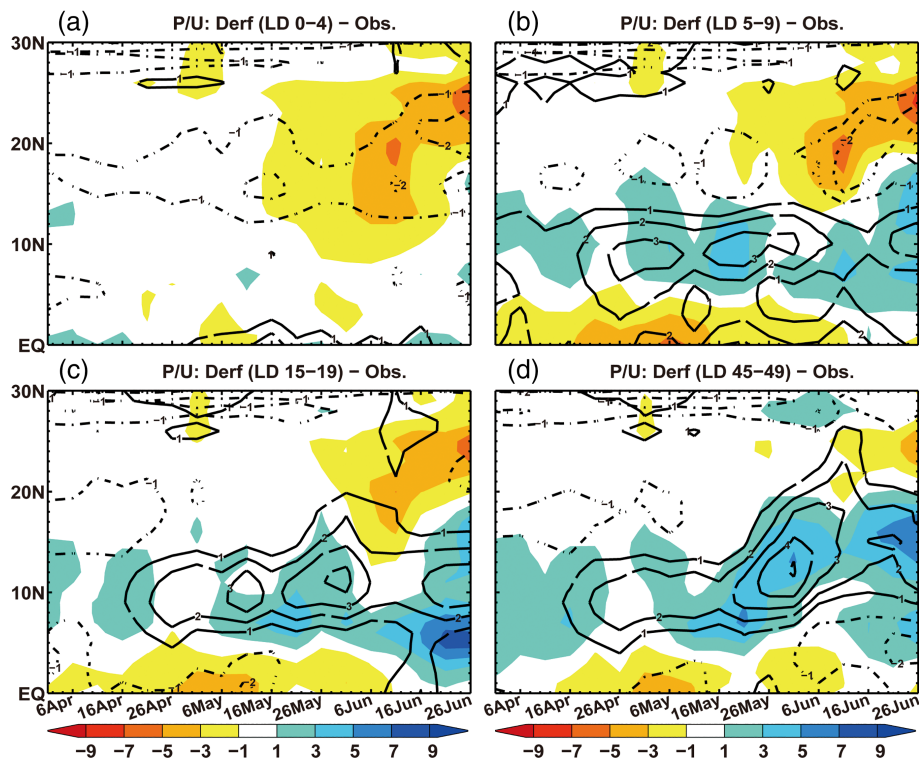
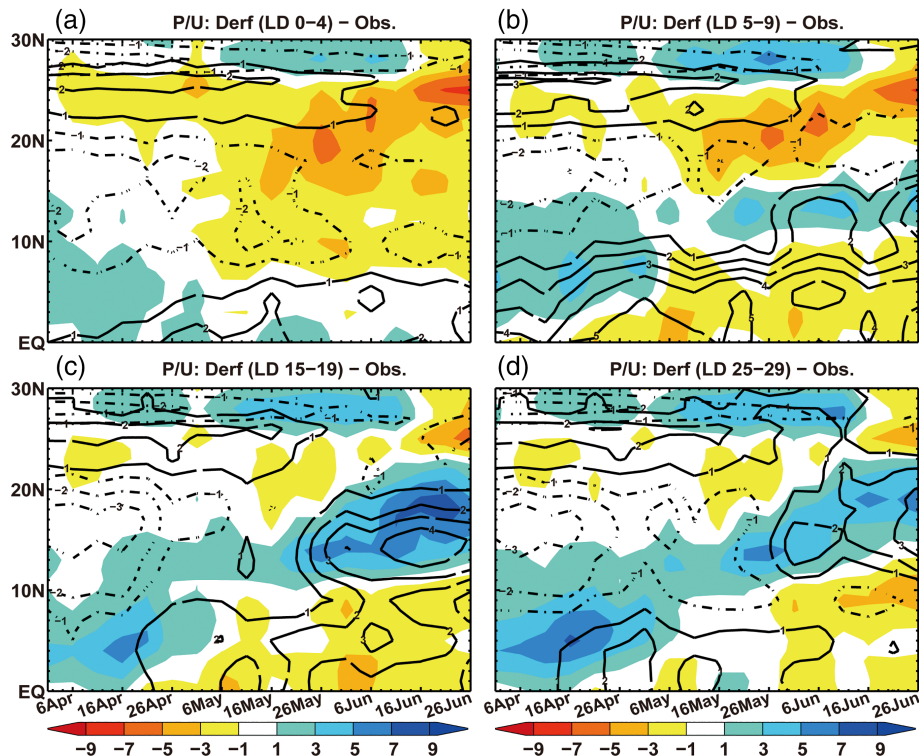


**FIGURE 6** Same as in Figure 5, except along  $90^\circ\text{--}110^\circ\text{E}$



of May, and the large values over  $20^\circ\text{N}$  afterward (not shown). However, differences appear between observations and model results, especially in the timing of BOB monsoon advancement and the position of rain belt. On the one hand, the centre of dry bias over  $20^\circ\text{--}30^\circ\text{N}$

gradually diminishes with increasing lead time from mid-May. On the other hand, all time leads except for 0–4 days show a wet bias belt, which begins from the equatorial area and shifts northward to the Asian continent during April–June. The forecasted winds (contours)

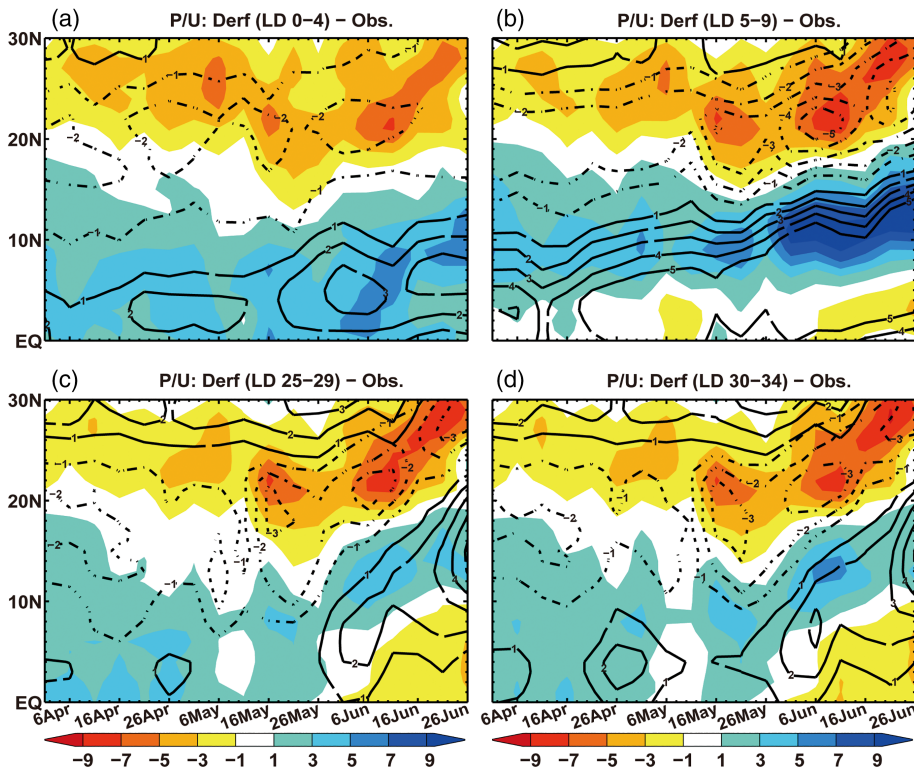


**FIGURE 7** Same as in Figure 5, except along  $110^{\circ}$ – $130^{\circ}$ E

at various leads show not only a good agreement with observations (e.g., northward shift), but also a small difference in wind speed from the observed. Other important features include the westerly and easterly biases over  $10^{\circ}$ – $20^{\circ}$ N at 0–4 lead days and the northward-shifting westerly biases near the equator, later on, followed by dominant westerly biases over  $10^{\circ}$ – $20^{\circ}$ N at 15–19 lead days in mid-May, where rainfall is overestimated (Figures 3 and 4). Overall, the variation of the difference between forecasted and observed winds is consistent with that of precipitation difference.

Similar to the spatial distributions on monthly and pentad time scales discussed previously, precipitation centres appear over northern South China and the Yangtze River in early-April, which is the same as the ‘spring rain in the Yangtze River’ (Chen *et al.*, 2000). However, there is a dry bias of rain belt over  $20^{\circ}$ – $30^{\circ}$ N, which intensifies significantly after the onset of SCSSM in the fifth pentad of May, when the 850-hPa zonal wind shows an easterly wind bias over  $20^{\circ}$ N. Interestingly, the wet biases from the equator to  $20^{\circ}$ N also become significant around the fifth pentad of May and move slightly northward. The difference between model and observation shows a maximum centre at 5–9 lead days, which diminishes from 10–14 to 25–29 lead days, followed by reinforcement from 30–34 lead days. Afterwards, the value of difference maintains with little change (Figure 7d). The westerly wind bias at 850 hPa is similar to that of precipitation from the equator to  $20^{\circ}$ N, but the position is

slightly different, especially for 5–9 lead days. Thus, we can conclude that the time of deviation change is exactly the same as the onset and northward movement of the SCSSM, but it is more significant at longer leads (Figure 7c,d). These results further demonstrate that the model can capture the commencement, development, and advancement of the ASM, but show poor forecast skill for the magnitude of wind and rainfall in some places.

### 3.3 | Prediction skill for spatial and temporal variability of regional rainfall

We select five domains (South China, ICP, BOB, SCS and IP; see Figure 8) to depict the regional features and prediction skills and analyse the main sources of errors. Figure 9 shows the Taylor diagrams of area-averaged precipitation and 850-hPa zonal wind at all leads. In general, the predictions of precipitation at all lead days are significantly correlated with observations. The predictions of short leads reasonably capture the features of sub-seasonal variations, and the rainfall predictions are highly correlated (dotted blue line) with observation for all leads, with a correlation coefficient above 0.9 in all regions except South China and the SCS, where the coefficients are 0.52–0.91 and 0.85–0.96, respectively. The root-mean-square errors (RMSEs; dotted green line) are 1.0–2.0 overall the five regions; however, the standard

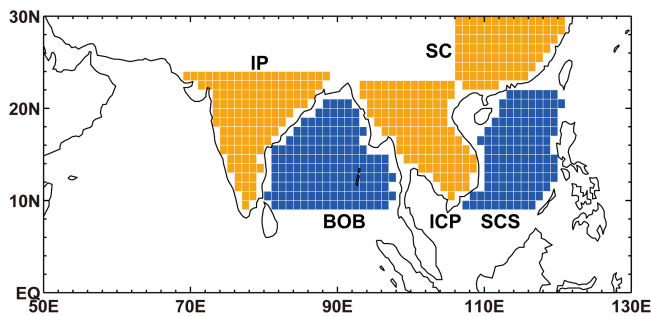


**FIGURE 8** Studied ranges of land domains (yellow; Indian subcontinent: IP, Indo-China Peninsula: ICP, and South China: SC) and ocean domains (blue; Bay of Bengal: BOB and South China Sea: SCS) in this article

deviation (STD; dotted black line) of each lead time over South China is smaller than observed. The small STD may be due to the underestimate of rainfall over South China as shown in Figures 3 and 4. On the other hand, there are larger differences between different leads over other regions, where the STDs have their minimum values only at the 0–4 lead days and 5–9 days (except for the SCS). For 850-hPa zonal wind, the forecast skill is much poorer over South China where the correlation coefficients between observation and model at some leads are even negative (not shown). The prediction skills of wind show larger consistency compared to those of rainfall, implying that the correlation coefficients are higher (above  $\sim 0.9$ ) and the RMSEs are smaller (below 2.0). STDs exhibit minimum values at the leads of 0–4 and 5–9 days.

Overall, the RMSEs, STDs and correlation coefficients of regional precipitation and zonal wind are not always the smallest at the minimum lead time. The forecast skill, which generally decreases with lead time, can increase again after the lead time is longer than 30 days, perhaps because the initial atmospheric memory has been lost significantly at that lead time and the predictions begin to be dominated by slowly-varying components of the climate system (Figures 5–7).

ACC is a more rigorous method for climate model evaluation, which allows us to analyse the forecast skills of models. In Figure 10, the model hindcast at the leads of 0–4 days shows better correlation with observations than at other leads in the other pentads from April to June, especially over the SCS where ACC is higher than 0.3. These results further demonstrate the reasonable skill of the model in forecasting the rainfall over SCS and the tremendous difficulty in forecasting the rainfall over South China. Meanwhile, the ACCs decrease rapidly or even show negative values with lead time over South China. Similar to Figures 5–7 and 9, the ACCs of most

target pentads do not decrease progressively with lead time, but ‘decrease’ and ‘increase’ alternately over each region. For example, the obvious change in ‘decrease–increase–decrease’ can be seen in the third pentad of April over IP, ICP, and BOB. Overall, the best correlations between forecasts and observations are seen in April for all five regions, especially in the second, third, and fifth pentads of April, followed by May, and the worst is in June.

For rainfall anomalies, the PCCs between observation and model results are computed pentad by pentad, and year by year. Figures 11, 12 show the multi-year-averaged PCCs in each pentad and during spring-to-summer transition for each year. Climatologically, there are higher skills over IP and BOB than over the other regions. In addition, the PCCs decrease with increasing lead time over South China, IP, ICP, and BOB. Note that the PCC of SCS rainfall exhibits two maximum periods, the third pentad of May and after mid-June. PCCs can be predicted skillfully at the leads of 0–4 days in all pentads over all regions, and they also decrease or show ‘high-low’ oscillation with increasing lead time (Figure 11). Corresponding with Figure 11, the spring-to-summer averaged PCCs in each year exhibit more remarkable inter-annual differences over IP and BOB, featured by a fast drop of PCC below the confidence level after a few days of forecasts in some years but at about 3-week or longer leads in the other years (Figure 12). Over IP, the skills are significant at the 40-day-lead time for forecasts of most years. In contrast, over South China, ICP, and SCS, relatively small inter-annual differences in PCC are found, along with a rapid drop of PCC below the 95% confidence level in most years (Figure 12).

### 3.4 | Possible causes of prediction biases

The above analysis indicates that the skills of sub-seasonal prediction of the onset, development, and prevalence of the ASM depend on both lead time and the evolution stage of the monsoon. On the one hand, the bias of rainfall prediction shifts northward as the rain belt moves northward (see Figures 5–7). The bias shows a significant change from mid-May onward, especially after the fifth pentad of May. Meanwhile, the prediction of zonal wind shows a similar feature, but there is a remarkable dissimilarity in the position of bias with rainfall prediction, especially near the equator and the western Pacific tropical monsoon region (Figure 7). On the other hand, biases do not always increase with increasing lead time, and are not consistent in different regions and at different leads, which to some extent agrees with the features shown in Figures 5–7. Therefore, it is necessary to answer the question of what results in these features.

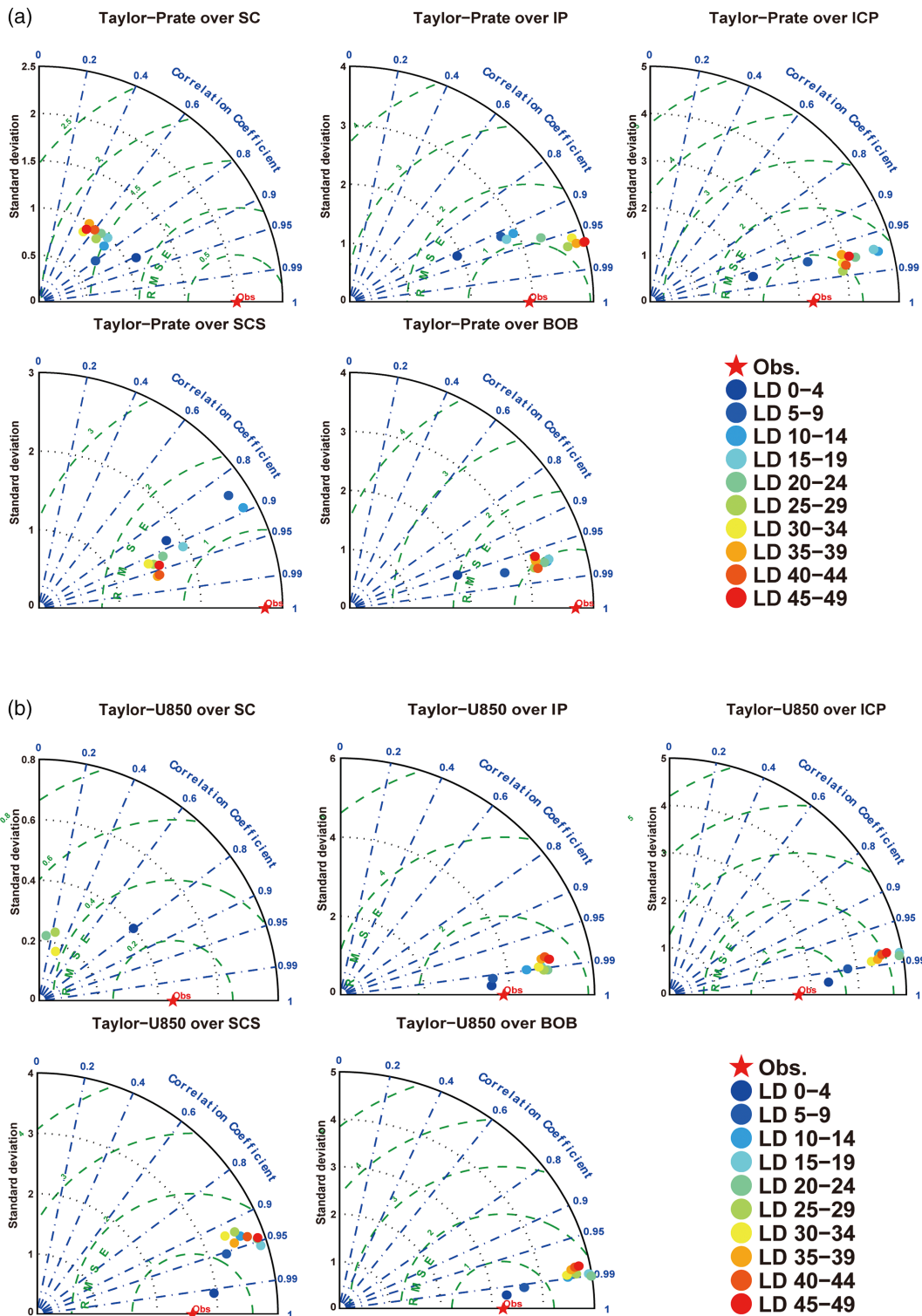


**FIGURE 9** Taylor diagrams of standard deviation, temporal correlation coefficient, root-mean-square error (RMSE) between ensemble prediction and observation for (a) precipitation (units:  $m \cdot s^{-1}$ ) and (b) 850-hPa zonal wind (units:  $mm \cdot day^{-1}$ ) over the Indo-China Peninsula (ICP), Bay of Bengal (BOB), South China Sea (SCS), Indian subcontinent (IP), and South China (SC)

As suggested in Sections 3.1–3.3, the NWP is dominated by cyclonic wind bias and the associated precipitation bias, which may be closely associated with the

WPSH, bridging tropical SST anomalies and the change in East Asian summer circulation. That is, the deviations of forecasted WPSH may exert an impact on the

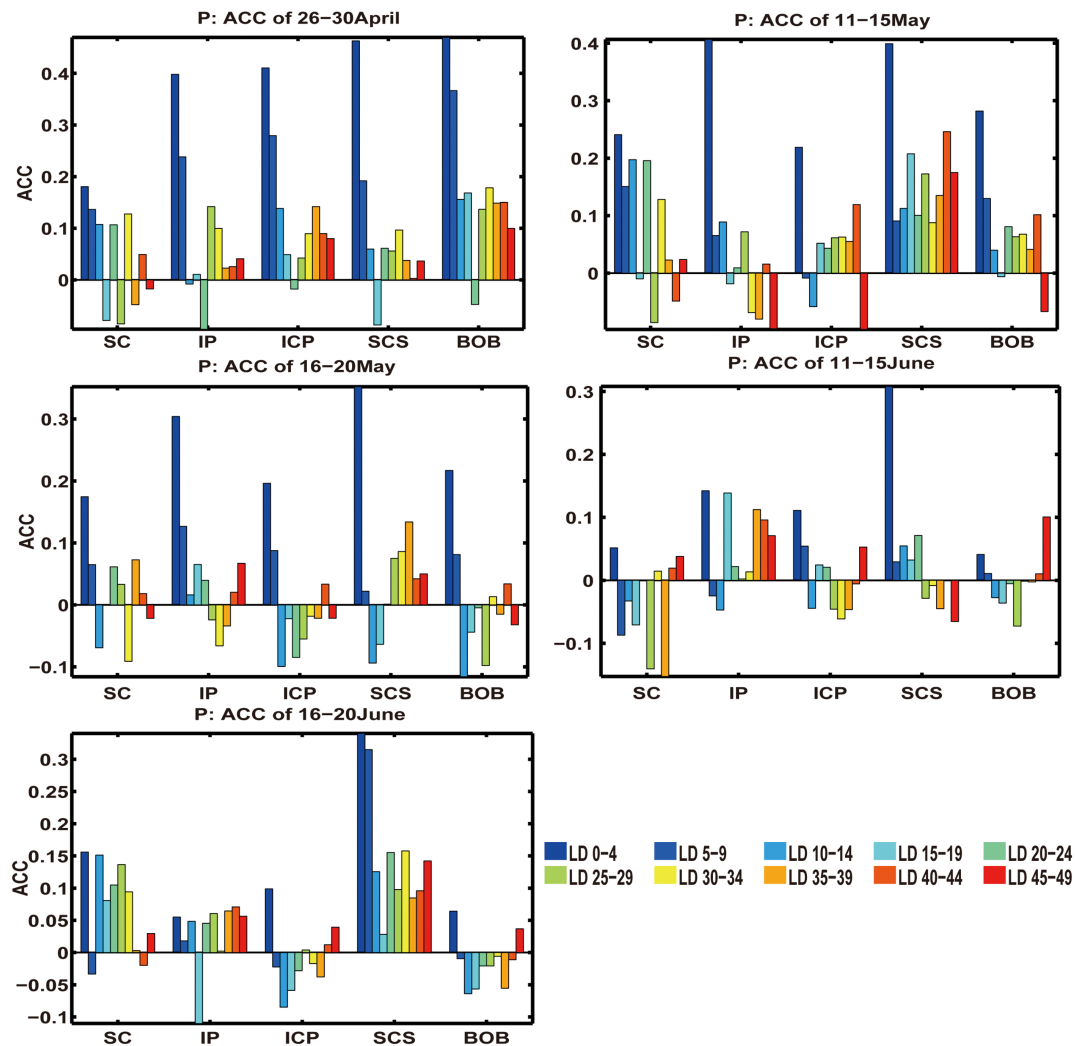


**FIGURE 10** ACC skills of pentad rainfall predictions at various lead times with respect to observations averaged over the South China (SC), Indian subcontinent (IP), Indo-China Peninsula (ICP), South China Sea (SCS), and Bay of Bengal (BOB)

magnitude and distribution of rainfall and the advance of rain belt in East Asia. Figure 13a shows the variation of WPSH ridge, defined as the average latitude of zero contour of 850-hPa zonal wind within  $120^{\circ}$ – $150^{\circ}$ E/ $10^{\circ}$ – $45^{\circ}$ N, in the ensemble mean predictions at different leads. The ridge shows an early and slowly southward retreat or a northward jump as lead time increases. Model predictions capture the observed features of sub-seasonal change but show larger differences in magnitude. In the meantime, the observed WPSH ridge jumps northward accompanied by the outbreak of the SCSSM after the fifth pentad of May, but model predictions show more southward than observations at all lead days except for 0–4 lead days. Compared with observation, the predicted WPSH ridge is mostly more northward before the fifth pentad of May and more southward after the fifth pentad of May. However, the model skill does not progressively

decrease with increasing lead time, especially before late-May.

Figure 13b shows the variation of the Webster–Yang (WY) index, which is defined as the vertical shear of zonal winds between 850- and 200-hPa levels averaged over  $40^{\circ}$ – $110^{\circ}$ E/ $0^{\circ}$ – $20^{\circ}$ N (Webster and Yang, 1992). The WY monsoon index represents well the South Asian monsoon (tropical monsoon), while WPSH is a major member of the subtropical monsoon system. The correlation coefficient between the WY index and the WPSH ridge index is  $-0.55$  in observation, exceeding the 95% confidence level. The two indexes jointly characterize the ASM. The WY index is defined as the vertical shear of zonal winds between 850- and 200-hPa levels averaged over  $40^{\circ}$ – $110^{\circ}$ E and  $0^{\circ}$ – $20^{\circ}$ N, which is located in the southwest of WPSH. So the position of WPSH is closely related to the strength of the South Asian monsoon. The

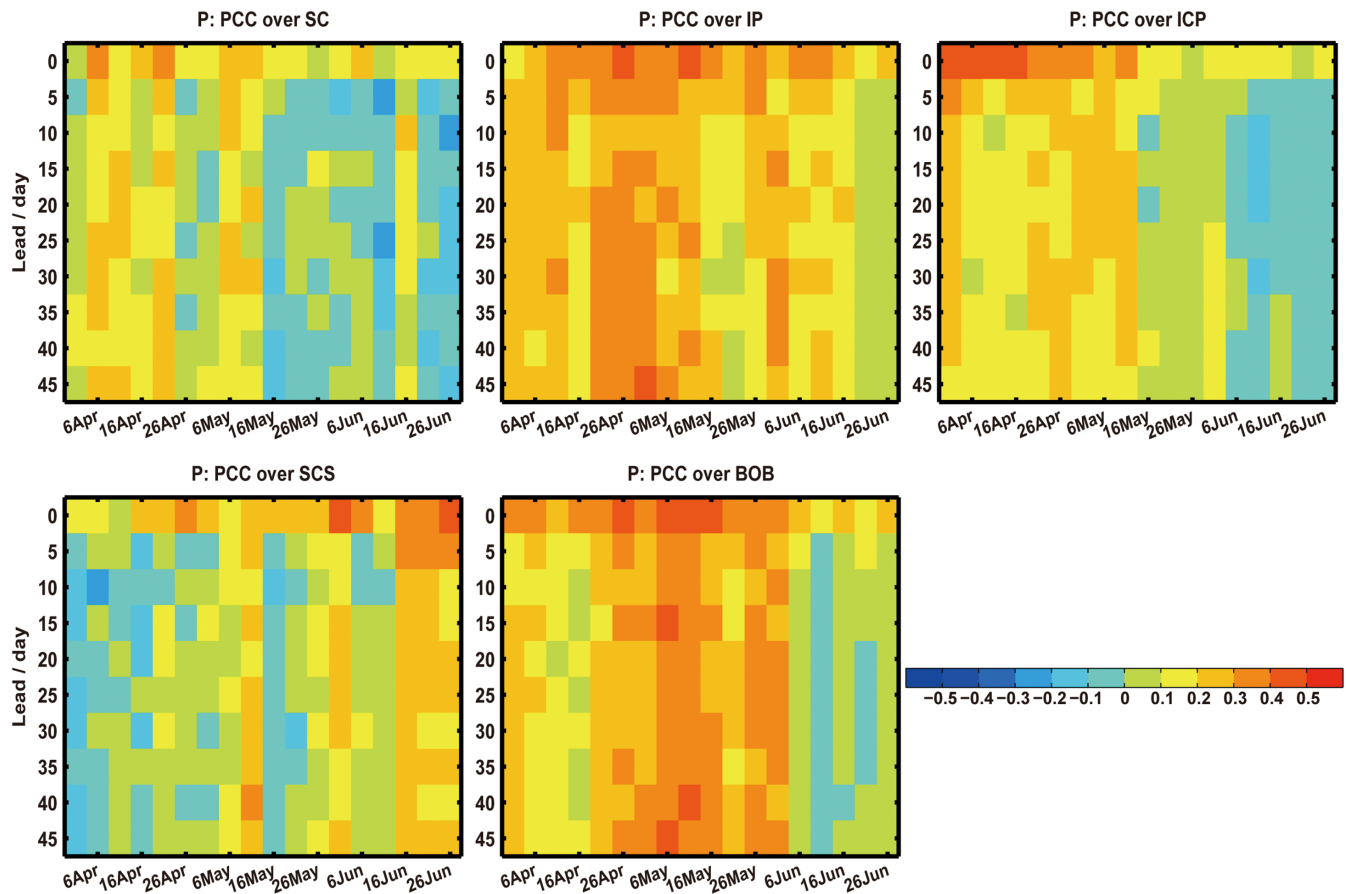


**FIGURE 11** Multi-year-averaged PCCs between forecasted and observed rainfall over the South China (SC), Indian subcontinent (IP), Indo-China Peninsula (ICP), South China Sea (SCS), and Bay of Bengal (BOB) as a function of lead time ( $y$  coordinate) and seasonal stage ( $x$  coordinate)

significant negative correlation between the two indexes indicates that when the South Asian summer monsoon is strong, the WPSH ridge is southward, and the subtropical summer monsoon is weak.

The predicted WY index is more consistent with observation than the WPSH ridge index during the entire analysis period, but it shows a systematic weak bias since early-June except before late-May. Meanwhile, the predicted WY index is weaker at the lead time of 15–19 and 20–24 days but stronger at the lead time of 0–4 and 5–9 days. Model predictions exhibit more consistency with observations for short leads (such as 0–4 days) than for long leads (such as 20–24 days) within the lead time less than 30 days. It approves that the correlation between prediction and observation decreases with lead time (for less than 30 days, Figure 9) and that the 0–4 day-lead prediction is in good agreement with observation (Figure 10).

Both internal atmospheric variability and external forcing may contribute to model biases and their growth. To further understand the differences between prediction and observation, we analyse latitude-time cross sections

(Figure 14) for ensemble-mean prediction biases of surface temperatures at different leads along  $110^{\circ}$ – $130^{\circ}$ E including SCS and South China. The development of thermal bias exhibits apparently spatial and temporal differences. The change in significant bias is mainly concentrated near  $20^{\circ}$ – $30^{\circ}$ N, with the cold bias near  $30^{\circ}$ N before May gradually replaced by a warm bias after May, corresponding to the change from a cold to a warm bias south of the Yangtze River from April to June (Figure 2). The warm bias enhances gradually from 0–4 lead days to 15–19 lead days, and then weakens from 20–24 lead days to 30–34 lead days, before gradually intensifying again from 35–39 lead days to 45–49 lead days. Interestingly, the model warm biases at all leads except for 0–4 lead days become significant from mid-May, especially from the fifth pentad of May (Figure 11), associated with the apparent southward-shifted WPSH ridge and the weak WY index in various lead-time predictions after mid-May (Figure 13). In the meantime, the warm bias over  $20^{\circ}$ – $30^{\circ}$ N gradually expands northward to  $35^{\circ}$ N around late-June, related to the northward movement of the WPSH (Figure 13a).

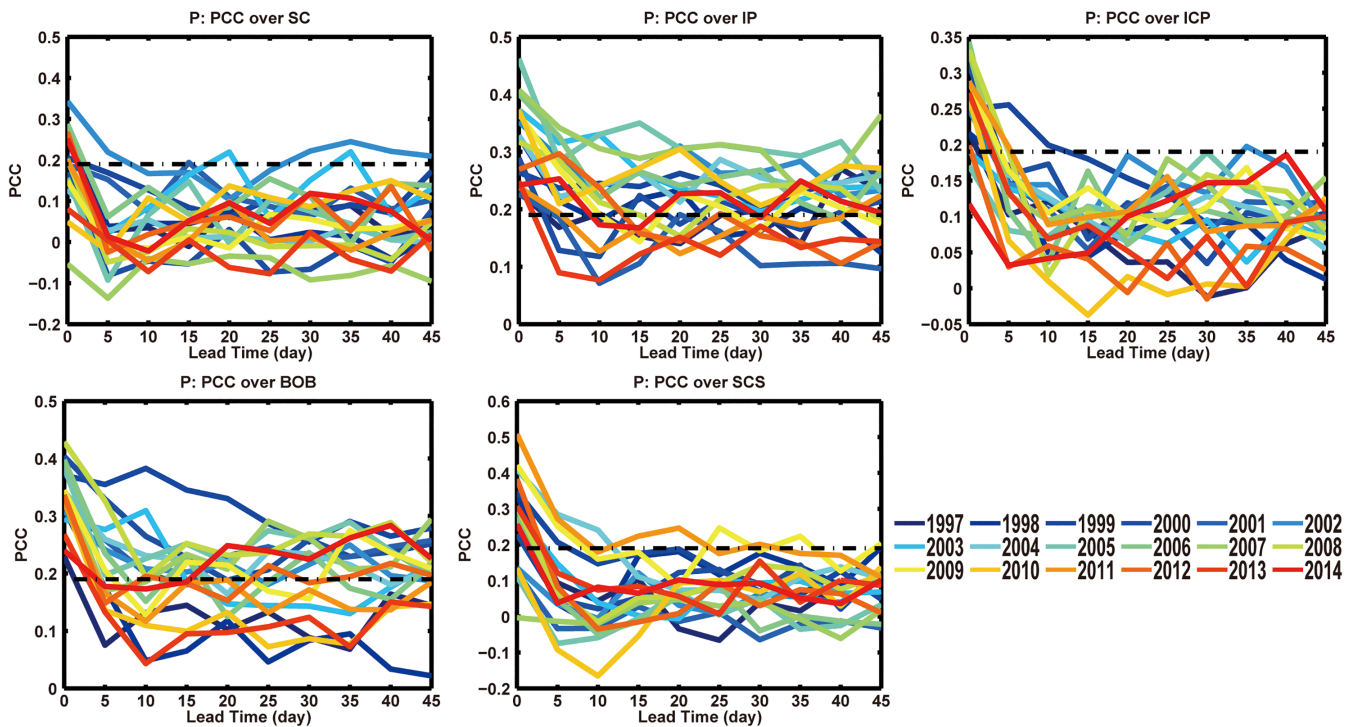


**FIGURE 12** April–June averaged PCCs between forecasted and observed rainfall over the South China (SC), Indian subcontinent (IP), Indo-China Peninsula (ICP), South China Sea (SCS), and Bay of Bengal (BOB) as a function of lead time ( $x$  coordinate) for each year. The black dashed line denotes the statistically significant value at 95% confidence level (Student's  $t$  test)

To link all these known factors and gain a more comprehensive understanding of the causes for prediction biases, an MV\_EOF analysis is carried out for precipitation and 850-hPa winds (Figure 15), and for surface temperature and 850-hPa winds (Figure 16). The first EOF mode and principal components (PCs) of precipitation and winds (Figure 15) show that the bias distribution clearly transits from the negative phase to the positive phase around mid-May, from the third pentad to the fifth pentad of May, which occurs earlier in short-lead predictions than in long-lead predictions. The transition corresponds to the split time when the WPSH ridge and the SKT between  $20^{\circ}\text{N}$  and  $30^{\circ}\text{N}$  (such as South China) show significant changes (Figures 13a and 14). Associated with the positive phase beginning in mid-May, the first mode is characterized by the development of cyclonic wind biases over the NWP, and westerly wind biases over the ICP and the southwestern IP where wet biases exist. On the other hand, anticyclonic wind biases occur over the western tropical IO and Somali, and northwesterly wind biases exist over the equatorial IO and from the northeastern ICP to the equatorial region through the BOB. Correspondingly, dry biases appear over the equatorial IO, the northeastern IP and BOB, and other equatorial regions. In addition, precipitation is underestimated over the west coast of the NWP, including the Kuroshio, South

China, and the SCS, which may be related to the northwesterly or northeasterly wind bias caused by the cyclonic bias over the NWP. As discussed in Sections 3.1 and 3.2, these biases indicate weak WPSH and South Asian summer monsoon. Along with the similar distribution of wind biases revealed in Figure 15c and the associated with the positive phase beginning in mid-May, the first EOF modes of SKT and winds (Figure 16c) show apparent cold biases over the NWP and warm biases over the IO, which may be a response to the cyclonic wind bias over the NWP and the anticyclonic wind bias over the western tropical IO, respectively. Other apparent features include the cold biases and overestimated rainfall over the western IP and ICP, while there are warm biases from North Africa to East China, except for part of the TP.

Note that the first modes in Figures 15c and 16c are highly significant, explaining nearly 40% of the total variance. The negative phase of the spatial mode shown in Figure 15c bears much resemblance to the biases over the BOB and the SCS-WP ITCZ in April (see Figure 1c), and in the leads of 25–29 and 45–49 days in the sixth pentad of April (see Figure 4b,d). The positive phase of the spatial mode is similar to the bias distribution in June (see Figure 1i) and in the 25–29 and 45–49 lead days of the fourth pentad of June (see Figure 4n,p). In Figure 16c,

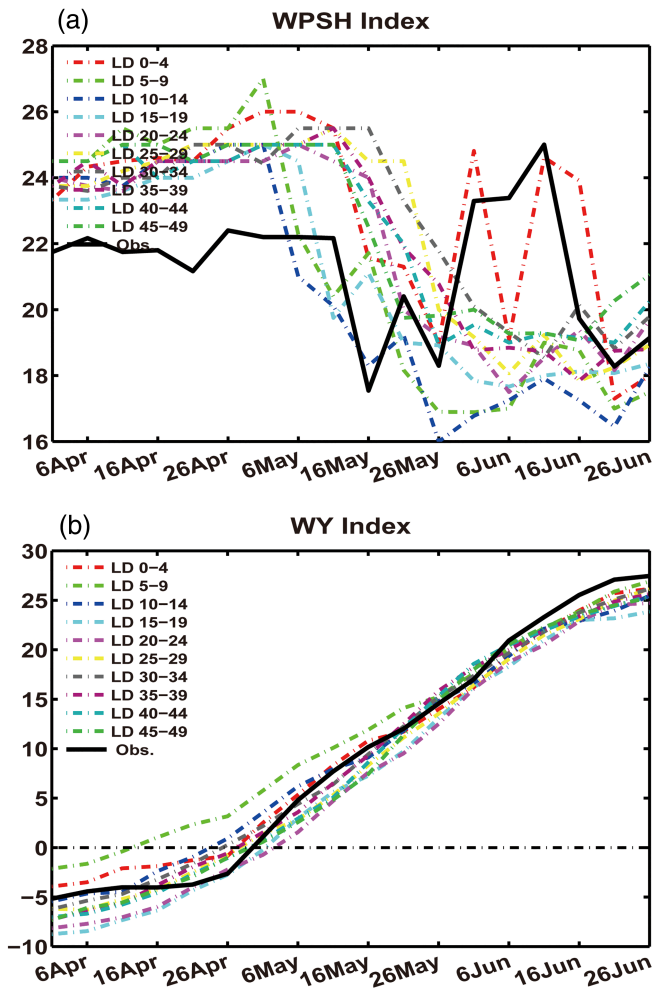


**FIGURE 13** Time series of ensemble predicted and observed ridges of the WPSH (a) and the Webster–Yang index (b) in the spring–summer transitional season (April–June)

the distribution of surface temperature biases over south of the ICP is opposite to that over south of China, as shown in Figure 2a,c. Therefore, the first mode may be related to the transitions of atmospheric circulation and the thermal state of the underlying surface. On the one hand, the WPSH with an anticyclonic wind bias before mid-May can contribute to the southeasterly or southwesterly wind bias to the west coast of the NWP but that with a cyclonic wind bias after May can intensify the northwesterly wind bias from South China to the equatorial regions. Associated with the evolution of wind bias, the precipitation and surface temperature biases over the NWP are replaced by opposite-sign biases during the transition process. On the other hand, the transition from anticyclonic biases to cyclonic biases over the western tropical IO and Somali regions may be closely connected with the regional surface temperature biases and partly attributed to the significant

change in surface temperature from warm to cold bias over the western IP (see Figures 2 and 16a,c). These features are favourable for the meridional wind biases over western IP changing from southerly to northerly wind bias as a thermal response of regional atmospheric circulation.

The second EOF modes and PCs of precipitation and winds (see Figure 15b,d), and of surface temperature and winds (see Figure 16b,d), show a consistent variation with a gradually increasing tendency from April to mid-May and a decreasing tendency from mid-May to June. Compared to the long-lead predictions, the PCs of short-lead predictions show smaller values but earlier peaks. The latter indicates an earlier northward jump of the WPSH as shown in Figure 13a, while the former indicates a decay of initial memory and a growth of prediction bias. The time range of transition from an ascending tendency to a descent tendency of all-lead predictions from the third pentad of May to the fifth pentad of May is consistent with that of the transition from a negative phase to a positive phase in Figures 15a and 16a. Otherwise, the transition from the negative phase to the positive phase around mid-April (Figures 15b and 16b) also corresponds to the split time when the WY index changes from a negative phase to a positive phase (Figure 13b). Associated with the positive phase from mid-April to mid-June (Figures 15b and 16b), the second mode is characterized by an apparent anticyclonic wind bias over the NWP and Somali-IO regions. Correspondingly, dry biases appear over the NWP, SCS, and IO. Apparent wet and warm biases south of China arise as a response to the southwesterly wind biases caused by the anticyclonic wind bias over the NWP. Meanwhile, wet and cold biases occur south of the ICP and northeast of the IP. Therefore, the second mode in the positive phase features a strong WPSH over the NWP and strong monsoon over South Asia. The biases associated with the second mode gradually intensify before the strongest SCSSM develops and the WPSH fully dominates over the NWP, and weaken as both SCSSM and WPSH move northward.

It should be noted that the second mode only accounts for 11% of the total variance and its typical features can be captured only when it is in a strong state and the first mode is in a weak state. For example, the positive phase of spatial mode shown in Figure 15d is similar to the bias distribution depicted in Figures 1f and 4h,l, which bears much resemblance to the biases south of China, the western Pacific, and Southeast Asia. Moreover, as pointed out above, biases do not always increase with increasing lead time. Knowing the time when biases reach their saturation state is helpful for identifying their causes. As shown in Sections 3.1 and 3.2, bias development depends on both lead time and the stage of

**FIGURE 14** Latitude-time cross sections of prediction biases of skin temperature (units: °C) along 110°–130°E. (a), (b), (c), and (d) for 0–4, 5–9, 15–19, 45–49 lead day prediction, respectively

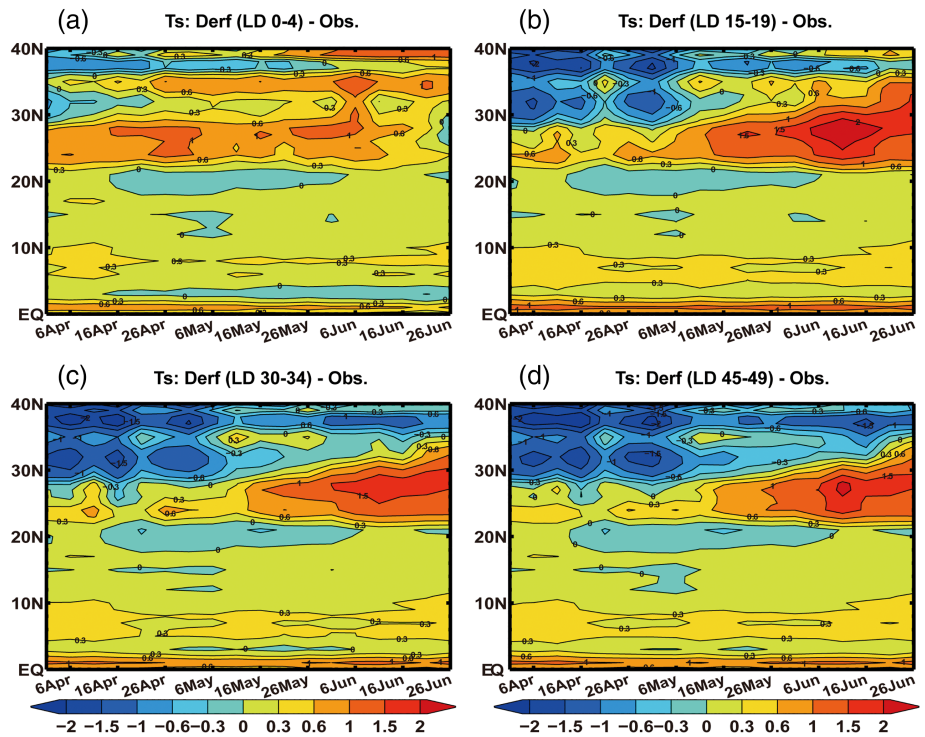
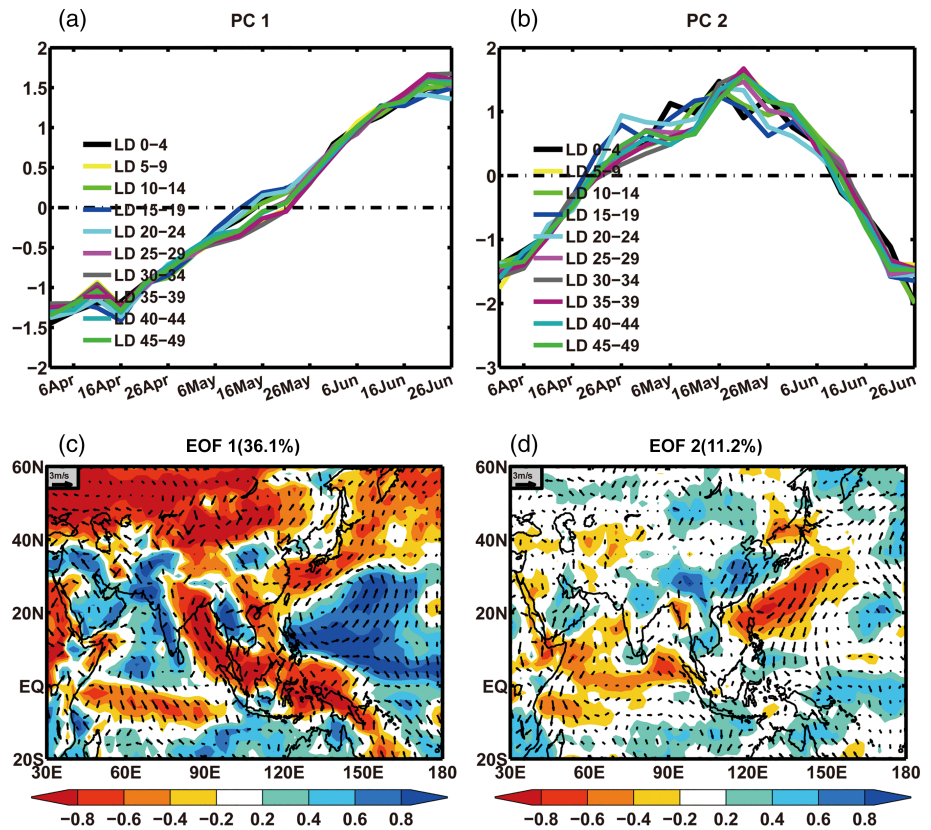


**FIGURE 15** The first two leading modes (bottom panels) and corresponding principal components (top panels) of multivariate EOF analysis on prediction biases of precipitation and 850-hPa wind at all lead times from 0 to 49 days. The value in parentheses on top of each panel in (c) and (d) represents the explained variance of each mode



monsoon evolution. In addition, significant geographical differences in bias growth with increasing lead time may result from different initial memory capabilities of the model over different regions. Figures 15 and 16 further

confirm that the predictions of different leads always show significant differences in the transition of biases. However, better consistency among the predictions of different leads may exist during other periods, which can

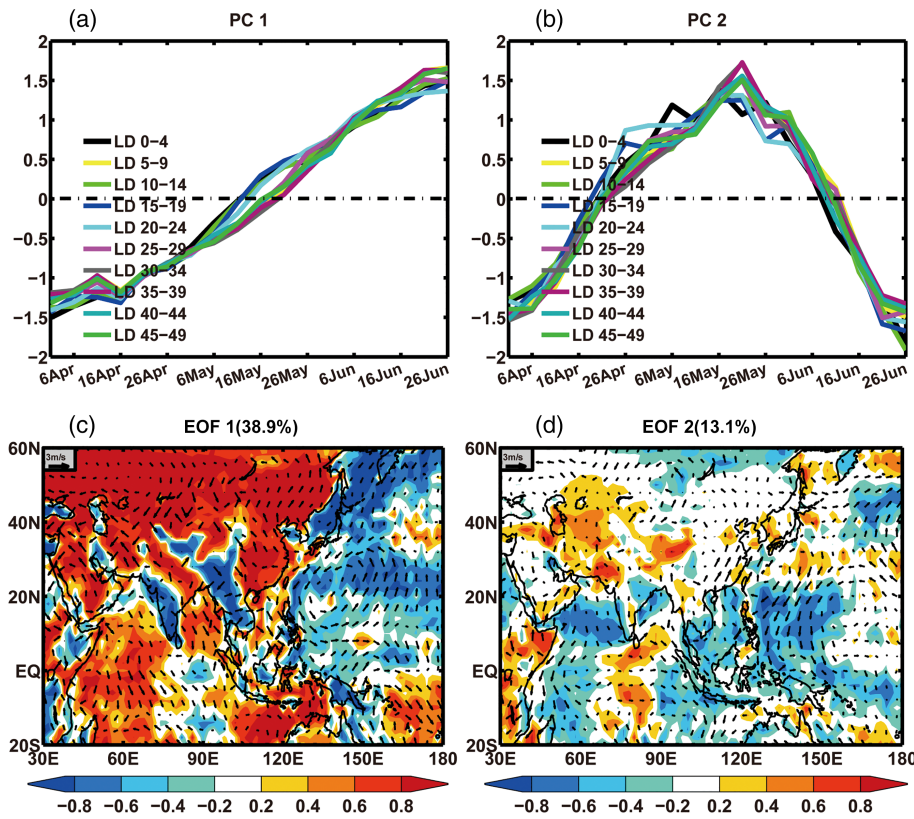


**FIGURE 16** Same as Figure 15, except for multivariate EOF analysis based on the biases of skin temperature and 850-hPa wind

partially result from the model responses to the biases of different components at different time leads.

#### 4 | CONCLUSIONS AND DISCUSSIONS

Based on the hindcasts of DERF2.0 from 1983 to 2014, the prediction skills of precipitation over the Asian monsoon region during the spring-to-summer transition (April–June) are examined. The key factors influencing the prediction skills are also explored. The study yields the following main conclusions:

1. The DERF2.0 can reproduce the observed distributions and sub-seasonal processes of precipitation, temperature, and 850-hPa winds, reflect the changing trend of the ASM during the spring-to-summer transition and generally capture the processes of onset and evolution of the East Asian summer monsoon. Thus, the DERF2.0 is skillful in predicting precipitation, SST, and winds during the spring-to-summer transition. However, the model still needs improvement in predicting the position and intensity of anomaly centres. For instance, the model has difficulties in predicting the abrupt increase or decrease in precipitation at most lead days, and the emergence of spurious

interruption at some leads. The underestimate of precipitation is found in the ITCZ over the SCS, the western Pacific, and the Meiyu rain belt.

2. Based on the ACC and PCC skills of precipitation, the model has high prediction skills for the IP and BOB, but relatively low skills for South China. The lower skill of the model in predicting rainfalls over South China compared to other regions is related to the poor skill of predicting WPSH. The prediction skill is best in April, followed by May, and worst in June. Biases are related not only to lead time but also to the stage of monsoon evolution. The model shows better prediction skills at 0–4 lead days, and afterwards bias becomes significant gradually. In general, model prediction skill decreases with increasing lead time when lead time is less than 30 days, but increases when lead time is longer than 30 days. An abrupt turning point of bias development appears in mid-May, when the bias growth of winds and precipitation shows significant changes over the NWP and the South Asian summer monsoon region, especially the BOB and the SCS. Otherwise, the location of the predicted WPSH ridge is more northward before the fifth pentad of May and southward afterwards compared with observation. The predicted WY index is also weaker than observed after mid-May.
3. The possible physical causes of biases are explored by using an MV\_EOF analysis method. The abrupt change

in the biases of winds, precipitation, and surface temperature is captured by the first two MV\_EOF modes. The first mode shows a transition from a negative phase to a positive phase in mid-May. Associated with the positive phase beginning in mid-May, the first mode is featured by weaker South Asian summer monsoon and WPSH compared to observations. The fundamental change depicted in the first mode also occurs around the split time mentioned above. The second EOF mode indicates an initial increasing tendency and then a decreasing tendency with a change in mid-May. The biases associated with this mode gradually intensify before the strongest SCSSM occurs and the WPSH fully dominates over the NWP, and weaken as the SCSSM and WPSH move northward. The positive phase features a strong WPSH over the NWP and a strong monsoon over South Asia. The transition from negative phase to positive phase in mid-April also corresponds to the split time when the WY index changes from negative phase to positive phase.

It is also found that the westerly wind in DERF2.0 is weaker than observation over most East Asia during the spring-to-summer transition, which results in less water vapours transported by westerly and southwesterly flows to eastern China in the model. It may be one of the leading causes of the weakly predicted precipitation over the East Asian monsoon region. The negative deviation of forecasted temperature over the TP and its surrounding regions is greater than that over the oceans to the east and south, which may affect the prediction of the intensity of monsoon circulation. Therefore, the biases of overestimated or underestimated monsoon precipitation by the DERF2.0 may be due to the influence of winds and surface temperature. Furthermore, are there any other causes for the errors of model simulations? How are they responsible for the performance of the rainfall forecast? To what extent can the conditions of local sea/land-atmosphere interactions and large-scale circulation pattern be skillfully reproduced?

Models' biases are associated with not only the initial errors but also the deficiency of models themselves. It is also found that there exist apparent spatial and temporal dependences on the proportion of the two (Lee and Krishnamurthy, 2010). In addition to the instability of the atmospheric system itself, the error growth of numerical prediction will amplify the initial error, plus another reason, that is, the increase in external error caused by model subsidence. All these problems need further investigations into the model's physical processes, land-sea-atmosphere interactions, and the effects of topography and sea temperature on the initial fields in order to improve both the model itself and its prediction skill.

## ACKNOWLEDGEMENT

This study was jointly supported by the Strategic Priority Research Program of Chinese Academy of Sciences (XDA20100304), the National Key Scientific Research Plan of China (2016YFA0602200 and 2013CB430202), the National Natural Science Foundation of China (41661144019), and the Jiangsu Collaborative Innovation Center for Climate Change.

## ORCID

Qingquan Li  <https://orcid.org/0000-0002-4133-6518>

Song Yang  <https://orcid.org/0000-0003-1840-8429>

## REFERENCES

- Abhilash, S., Sahai, A.K., Borah, N., Chattopadhyay, R., Joseph, S., Sharmila, S., de, S., Goswami, B.N. and Kumar, A. (2014) Prediction and monitoring of monsoon intraseasonal oscillations over Indian monsoon region in an ensemble prediction system using CFSv2. *Climate Dynamics*, 42(9–10), 2801–2815.
- Anderson, J.L. and Van, d.D.H.M. (1994) Skill and return of skill in dynamic extended-range forecasts. *Monthly Weather Review*, 122, 507–516.
- Chen, Q., Yu, Y. and Guo, Y. (1997) Simulation of east Asian summer monsoon with IAP CGCM. *Advances in Atmospheric Sciences*, 14(4), 461–472.
- Chen, L.X., Li, W., Zhao, P., Tao, S.Y. (2000). On the process of summer monsoon onset over East Asia. *Climate and Environmental Research*, 5(4): 345–355.
- Chen, S., Zhou, X., Lu, H., He, H. (2016) Temperature and precipitation evaluation of monthly dynamic extended range forecast operational system DERF2.0 in Guangxi. *Journal of Meteorological Research and Application*, 3, 16–19 [in Chinese].
- Ding, Y., Li, C., He, J., Chen, L., Gan, Z., Qian, Y., Yan, J., Wang, D., Shi, P., Fang, W., Xu, J. and Li, L. (2006) South China Sea monsoon experiment (SCSMEX) and the east Asian monsoon. *Acta Meteorologica Sinica*, 20(2), 159–190.
- Ding, Y., Liu, Y., Song, Y. and Li, Q. (2002) Research and experiments of the dynamical model system for short-term climate prediction. *Climatic and Environmental Research*, 7(2), 236–246 [in Chinese].
- Fu, X.H., Lee, J.Y., Hsu, P.C., Taniguchi, H., Wang, B., Wang, W. and Weaver, S. (2013) Multi-model MJO forecasting during DYNAMO/CINDY period. *Climate Dynamics*, 41(3–4), 1067–1081.
- He, H., Li, Q.P., Wu, T.W. (2014) Temperature and precipitation evaluation of monthly dynamic extended range forecast operational system DERF20 in China. *Chinese Journal of Atmospheric Sciences*, 38(5), 950–964.
- He, J.H., Zhao, P., Zhu, C., Zhang, R., Tang X., Chen, L. and Zhou, X. (2008) Discussion of some problems as to the east Asian subtropical monsoon. *Acta Meteorologica Sinica*, 22(4), 419–434.
- Huang, S. (1986). The rain storms in the pre-flood season in South China. Guangdong Science & Technology Press, 244.
- Huffman, G.J., Adle, R.F., Morrissey, M., Bolvin, D., Curtis, S., Joyce, R., McGavock, B. and Susskind, J. (2001) Global precipitation at one-degree daily resolution from multisatellite observations. *Journal of Hydrometeorology*, 2, 36–50.
- Johns, T.C., Durman, C.F., Banks, H.T., Roberts, M.J., McLaren, A. J., Ridley, J.K., Senior, C.A., Williams, K.D., Jones, A.,

- Rickard, G.J., Cusack, S., Ingram, W.J., Crucifix, M., Sexton, D. M.H., Joshi, M.M., Dong, B.W., Spencer, H., Hill, R.S.R., Gregory, J.M., Keen, A.B., Paradaens, A.K., Lowe, J.A., Bodas-Salcedo, A., Stark, S. and Searl, Y. (2006) The new Hadley Centre climate model (HadGEM1): evaluation of coupled simulations. *Journal of Climate*, 19(7), 1327–1353.
- Kalnay, E., Kanamitsu, M., Kistler, R., Collins, W., Deaven, D., Gandin, L., Iredell, M., Saha, S., White, G., Woollen, J., Zhu, Y., Leetmaa, A., Reynolds, R., Chelliah, M., Ebisuzaki, W., Higgins, W., Janowiak, J., Mo, K.C., Ropelewski, C., Wang, J., Jenne, R. and Joseph, D. (1996) The NCEP/NCAR 40-year reanalysis project. *Bulletin of the American Meteorological Society*, 77(3), 437–472.
- Lau, K.M. and Yang, S. (1997) Climatology and interannual variability of the southeast Asian summer monsoon. *Advances in Atmospheric Sciences*, 14, 141–162.
- Lee, D.H.K. and Krishnamurthy, V. (2010) Spatial structure, forecast errors, and predictability of the south Asian monsoon in CFS monthly retrospective forecasts. *Journal of Climate*, 23(18), 4750–4769.
- Lee, J.Y., Wang, B., Kang, I.S., Shukla, J., Kumar, A., Kug, J.S., Schemm, J.K.E., Luo, J.J., Yamagata, T., Fu, X., Alves, O., Stern, B., Rosati, T. and Park, C.K. (2010) How are seasonal prediction skills related to models' performance on mean state and annual cycle? *Climate Dynamics*, 35(2–3), 267–283.
- Li, H.L., Li, Q.Q., Wang, L.N., Dong, M. (2010) Trans-seasonal numerical prediction experiment of rainy season climate. *Scientia Meteorologica Sinica*, 30(6), 745–753 [in Chinese].
- Li, Q.Q., Ding, Y.H. and Zhang, P.Q. (2004) Primary verification and assessment on the extra-seasonally predictive capability of a global atmospheric-oceanic coupled model in raining season. *Acta Meteorologica Sinica*, 62(6), 740–751.
- Li, Q.Q., Zhang, R.H. and Liu, Y.M. (2015) Improvement of ocean data assimilation system and climate prediction by assimilating Argo data. *Journal of Tropical Meteorology*, 21(2), 171–184.
- Li, Q.Q. and Zhao, Z.C. (2002) Extra-seasonal predictions of summer rainfall in China and ENSO in 2001 by climate models. *Acta Meteorologica Sinica*, 16(4), 519–532.
- Li, Z.Y., Bai, H., Zhang, J., Wu, Z. (2017) Temperature and precipitation evaluation of monthly dynamic extended range forecast operational system in Guizhou. *Journal of Guizhou Meteorology*, 41(3), 1–9 [in Chinese].
- Liu, J., Xu, J.X., Ma, Z.F., Wu, T.W. (2014a) Evaluation of flood season prediction in southwest region by the second-generation monthly dynamic extended-range forecast. *Plateau Meteorology*, 33(6), 1468–1479.
- Liu, X., Yang, S., Kumar, A., Weaver, S. and Jiang, X. (2013) Diagnostics of subseasonal prediction biases of the Asian summer monsoon by the NCEP climate forecast system. *Climate Dynamics*, 41(5–6), 1453–1474.
- Liu, X., Yang, S., Li, J., Jie, W., Huang, L. and Gu, W. (2015) Subseasonal predictions of regional summer monsoon rainfall over tropical Asian oceans and land. *Journal of Climate*, 28(24), 9583–9605.
- Liu, Y. and Ding, Y. (2007) Analysis of basic features of the onset of the Asian summer monsoon. *Journal of Meteorological Research*, 21(3), 257–276 [in Chinese].
- Molteni, F., Cubasch, U. and Tibaldi, S. (1986) 30- and 60-day forecast experiments with the ECMWF spectral models. In: *Proc. ECMWF Workshop on Predictability in the Medium and Extended Range*. Reading, United Kingdom: ECMWF, pp. 51–107.
- Neena, J.M., Lee, J.Y., Waliser, D., Wang, B. and Jiang, X. (2014) Predictability of the Madden-Julian oscillation in the intra-seasonal variability hindcast experiment (ISVHE). *Journal of Climate*, 27(12), 4531–4543.
- Qi, L., He, J.H., Zhang, Z.Q. and Song, J.N. (2008) Seasonal cycle of the zonal land-sea thermal contrast and east Asian subtropical monsoon circulation. *Chinese Science Bulletin*, 53(1), 131–136.
- Reynolds, R.W., Rayner, N.A., Smith, T.M., Stokes, D.C. and Wang, W. (2002) An improved in situ and satellite SST analysis for climate. *Journal of Climate*, 15, 1609–1625.
- Simmons, A.S., Uppala, D.D. and Kobayashi, S. (2007) ERA-interim: new ECMWF reanalysis products from 1989 onwards. *ECMWF News*, 110, 29–35.
- Sperber, K.R. and Palmer, T.N. (1996) Interannual tropical rainfall variability in general circulation model simulations associated with the atmospheric model intercomparison project. *Journal of Climate*, 9(11), 2727–2750.
- Tang, H., Dong, X., Zhou, X., Qin, Z. (2016) Analysis and application of monthly dynamic extension forecast in Chongqing based on DERF2.0 data. *Desert and Oasis Meteorology*, 10(3), 1–8 [in Chinese].
- Uppala, S., Dee, D., Kobayashi, S., Berrisford, P. and Simmons, A. (2008) Towards a climate data assimilation system: status update of ERA-interim. *ECMWF News*, 115, 12–18.
- Webster, P.J. and Yang, S. (1992) Monsoon and ENSO: selectively interactive systems. *Quarterly Journal of the Royal Meteorological Society*, 118(507), 877–926.
- Wei, M., Li, Q.Q., Xin, X.G., Zhou, W., Han, Z., Luo, Y. and Zhao, Z. (2017) Improved decadal climate prediction in the North Atlantic using EnOI-assimilated initial condition in BCC\_CSM1.1. *Chinese Science Bulletin*, 62(16), 1142–1147.
- Wu, Q., Zhaobo, S., Baoshan, D., and Aihua, Z. (1994). Precipitation and circulation features during late-spring to early-summer flood rain in South China. *Journal of Nanjing Institute of Meteorology*, 17(4), 455–461.
- Wu, T.W., Yu, R.C., Zhang, F., Wang, Z., Dong, M., Wang, L., Jin, X., Chen, D. and Li, L. (2010) The Beijing Climate Center atmospheric general circulation model: description and its performance for the present-day climate. *Climate Dynamics*, 34(1), 123–147.
- Zhang, D.Q. and Chen, L.J. (2016) Bias correction in monthly means of temperature predictions of the dynamic extended range forecast model. *Chinese Journal of Atmospheric Sciences*, 40(5), 1022–1032.
- Zhao, P., Zhang, R.H., Liu, J.P., Zhou, X. and He, J. (2007) Onset of southwesterly wind over eastern China and associated atmospheric circulation and rainfall. *Climate Dynamics*, 28(7–8), 797–811.
- Zhou, T. and Yu, R. (2006) Twentieth-century surface air temperature over China and the globe simulated by coupled climate models. *Journal of Climate*, 19(22), 5843–5858.
- Zhou, T.J., Wu, B., Scaife, A.A., Brönnimann, S., Cherchi, A., Fereday, D., Fischer, A., Folland, C., Jin, K., Kinter, J., Knight, J., Kucharski, F., Kusunoki, S., Lau, N., Li, L., Nath, M., Nakaegawa, T., Navarra, A., Pegion, P., Rozanov, E., Schubert, S., Sporyshev, P., Voldoire, A., Wen, X., Yoon, J. and Zeng, N. (2009a) The CLIVAR C20C project: which components of the

- Asian-Australian monsoon circulation variations are forced and reproducible? *Climate Dynamics*, 33, 1051–1068.
- Zhou, T.J., Wu, B. and Wang, B. (2009b) How well do atmospheric general circulation models capture the leading modes of the interannual variability of the Asian-Australian monsoon? *Journal of Climate*, 22, 1159–1173.
- Zhou, T.J., Yu, R.C., Zhang, J., Drange, H., Cassou, C., Deser, C., Hodson, D., Sanchez-Gomez, E., Li, J., Keenlyside, N., Xin, X. and Okumura, Y. (2009c) Why the western Pacific subtropical high has extended westward since the late 1970s. *Journal of Climate*, 22, 2199–2215.
- Zhou, T.J. and Zou, L.W. (2010) Understanding the predictability of east Asian summer monsoon from the reproduction of land-sea thermal contrast change in AMIP-type simulation. *Journal of Climate*, 23(22), 6009–6026.
- Zhu, C.Z., Li, Q.Q., Wang, L.N., Wang, Z.Z. and Liu, W. (2013) An ensemble forecast for summer with a global atmospheric general circulation model T106L26. *Transactions of Atmospheric Science*, 36(2), 192–201 [in Chinese].

**How to cite this article:** Li Q, Wang J, Yang S, Wang F, Wu J, Hu Y. Sub-seasonal prediction of rainfall over the South China Sea and its surrounding areas during spring–summer transitional season. *Int J Climatol*. 2020;1–21. <https://doi.org/10.1002/joc.6456>